View metadata, citation and similar papers at core.ac.uk
brought to you by CORE
provided by Sussex Research Online

Mon. Not. R. Astron. Soc. **413,** 691–704 (2011) doi:10.1111/j.1365-2966.2010.18165.x

Baryon fractions in clusters of galaxies: evidence against a pre-heating model for entropy generation

Owain E. Young,[1⋆] Peter A. Thomas,[1] C. J. Short[1] and Frazer Pearce[2]

[1]*Astronomy Centre, University of Sussex, Falmer, Brighton BN1 9QH*
[2]*Department of Physics and Astronomy, University of Nottingham, Nottingham NG7 2RD*

Accepted 2010 December 7. Received 2010 November 2; in original form 2010 July 2

ABSTRACT

The Millennium Gas Project aims to undertake smoothed particle hydrodynamic resimulations of the millennium simulation, providing many hundred massive galaxy clusters for comparison with X-ray surveys (170 clusters with $kT_{\rm sl} > 3$ keV). This paper looks at the hot gas and stellar fractions of clusters in simulations with different physical heating mechanisms. These fail to reproduce cool-core systems but are successful in matching the hot gas profiles of non-cool-core clusters. Although there is immense scatter in the observational data, the simulated clusters broadly match the integrated gas fractions within r_{500}. In line with previous work, however, they fare much less well when compared to the stellar fractions, having a dependence on cluster mass that is much weaker than is observed. The evolution with redshift of the hot gas fraction is much larger in the simulation with early pre-heating than in one with continual feedback; observations favour the latter model. The strong dependence of hot gas fraction on cluster physics limits its use as a probe of cosmological parameters.

Key words: galaxies: clusters: general – galaxies: evolution.

1 INTRODUCTION

The hot gas fraction of clusters of galaxies was first used as a cosmological probe by Allen, Schmidt & Fabian (2002), and later refined in Allen et al. (2004) and Allen et al. (2008). These papers show quite conclusively that the gas fraction can be used to derive cosmological parameters that are in agreement with the concordance Λ cold dark matter (ΛCDM) cosmology. A similar result was obtained by LaRoque et al. (2006) in a joint X-ray, Sunyaev–Zel'dovich analysis. Subsequently, a more sophisticated analysis that properly takes into account selection effects, and combines mass, X-ray luminosity and temperature observations of 238 clusters at $z \leq 0.5$, reached similar conclusions (Mantz et al. 2009a,b), as did a study by Ettori et al. (2009) of 60 clusters extending to $z \sim 1.3$.

However, as has been pointed out by Sadat et al. (2005), the above conclusion relies very heavily upon the assumption that the gas fraction in the clusters used in the study is independent of both mass and redshift. We show in this paper that using different models for entropy generation in the intracluster medium (ICM) can lead to variations in hot gas fractions in simulated clusters that are at least as great as those that one obtains by using an incorrect cosmology in the observational data analysis. We argue, therefore, that, at present, it is more useful to fix the cosmology to the concordance value and to use the data to constrain cluster physics. By doing so, we conclude that the data favour a model of continual energy injection into the ICM from galaxies rather than a widespread pre-heating episode at high redshift.

In the future, once the physical models of the ICM become more refined, and with the large statistical samples of clusters generated by *eROSITA*, it should be possible to do a combined analysis that constrains both the cluster physics and the cosmology simultaneously.

In Section 2 we describe the numerical method that we use, the different feedback schemes and our method of cluster identification. Section 3 describes our results first on gas fraction profiles, then scaling relations and finally the evolution of each of these. The conclusions of the paper are summarized in Section 4.

2 METHOD

Here we present an overview of our numerical scheme. The method is described at length in Short & Thomas (2009) and its particular application to clusters of galaxies in Short et al. (2010).

2.1 Simulations

We present results from three simulations taken from the Millennium Gas Project, the basic objective of which is to add gas to the dark-matter-only millennium simulation (Springel et al. 2005). Each simulation incorporates a different model of the baryonic physics, so that we can assess the impact of varying physical assumptions on the thermal history of the ICM.

⋆E-mail: o.e.young@sussex.ac.uk

© 2011 The Authors
Monthly Notices of the Royal Astronomical Society © 2011 RAS

In the first Millennium Gas run, the intracluster gas is heated solely by gravitational processes. We refer to this simulation as the gravitation only (GO) run. Although this run does not include gas cooling or heating from astrophysical sources such as supernovae (SNe) and active galactic nuclei (AGNs), it is useful as a base model, enabling us to determine exactly which cluster properties are affected by astrophysical processes beyond gravitational heating. Given that the only source of gas entropy changes in the GO run is gravity, then we would expect a self-similar cluster population to be formed. This is generally found to be the case in non-radiative simulations (e.g. Navarro, Frenk & White 1995; Eke, Navarro & Frenk 1998; Voit, Kay & Bryan 2005; Ascasibar et al. 2006; Muanwong, Kay & Thomas 2006; Stanek et al. 2010).

The second Millennium Gas simulation also includes high-redshift pre-heating (first posited by Kaiser 1991; Evrard & Henry 1991) and radiative cooling. We name this simulation the pre-heating plus cooling (PC) run. Pre-heating raises the entropy of the ICM before gravitational collapse, preventing gas from reaching high densities in central cluster regions and thus reducing its X-ray emissivity. This effect is greater in lower mass systems, breaking the self-similarity of the cluster scaling relations in a way that resembles observations (Bialek, Evrard & Mohr 2001; Brighenti & Mathews 2001; Muanwong et al. 2002; Borgani et al. 2002; Tornatore et al. 2003; Borgani et al. 2005).

The simple model of pre-heating employed in the PC simulation is similar to that of Borgani et al. (2002). Briefly, the entropy of every particle is raised to 200 keV cm^2 at $z = 4$, thus creating an entropy 'floor' (note that a particle's entropy is not changed if it already has a value in excess of this at $z = 4$). In addition to pre-heating, there is also radiative cooling based on the cooling function of Sutherland & Dopita (1993), assuming a fixed metallicity of $0.3\,Z_\odot$ (a good approximation to the mean metallicity of the ICM out to at least $z = 1$; Tozzi et al. 2003). Once the temperature of a gas particle drops below 2×10^4 K, the hydrogen density exceeds $\rho_H = 4.2 \times 10^{-27}$ g cm^{-3} and the density contrast is greater than 100, then it is converted to a collisionless star particle. However, the pre-heating is so extreme that star formation is effectively terminated at $z = 4$, so that less than 2 per cent of the baryonic matter is locked up in stars at $z = 0$.

Although there is considerable evidence that non-gravitational heating of the ICM indeed occurs mainly at high redshift (e.g. Eisenhardt et al. 2008; Weiner et al. 2009), the pre-heating scenario is clearly a gross simplification of the complex interplay between star formation, black hole growth and associated feedback. Despite this, pre-heating does provide a useful effective model for the effects of non-gravitational heating. In particular, the Millennium Gas PC run can reproduce several key observational properties of the low-redshift cluster population, including halo gas fractions (Stanek et al. 2010). However, the model fails to account for the observed scatter about the mean relations, particularly on group scales, and generates overlarge isentropic cores in low-mass systems as compared to observational data (e.g. Ponman, Sanderson & Finoguenov 2003; Pratt, Arnaud & Pointecouteau 2006).

Finally, we use a recent addition to the Millennium Gas suite in which feedback is directly tied to galaxy formation, rather than assuming some ad hoc injection of energy at high redshift. We term this the feedback only (FO) run to emphasize the fact that the model currently does not include radiative cooling. The model we use is the hybrid scheme of Short & Thomas (2009), where a semi-analytic model (SAM) is used to calculate the energy transferred to the intracluster gas by SNe and AGN. An immediate benefit of this approach is that feedback is guaranteed to originate from a galaxy population whose observational properties agree well with those of real galaxies. This is generally not the case in fully self-consistent hydrodynamical simulations that include radiative cooling and stellar feedback because too much gas cools out of the hot phase, leading to excessive star formation (e.g. Borgani et al. 2004; Kay et al. 2007a). It is widely thought that additional heating from AGN is the natural solution to this overcooling problem. Indeed, McCarthy et al. (2009) and Fabjan et al. (2010) have demonstrated that including AGN feedback in hydrodynamical simulations can successfully balance radiative cooling in galaxy groups. However, the stellar fraction is still found to be 2 to 3 times larger than observed in massive clusters.

For reasons of computational efficiency, the FO run was not undertaken over the entire millennium simulation volume. Instead, we resimulated a sample of several hundred galaxy groups and clusters. Each run came in three distinct stages: a dark-matter-only resimulation of each region containing a cluster from our sample; semi-analytic galaxy catalogues built on the halo merger trees of these resimulations and hydrodynamical resimulations of the same regions to track the energy injection from model galaxies. The merger trees were built using the procedure of Springel et al. (2005), and we used the Munich L-Galaxies SAM with the same parameters as described in De Lucia & Blaizot (2007). Energy is injected into the ICM from both SNe and AGN following the prescription of Short & Thomas (2009). The procedure is described in full in Short et al. (2010)

By coupling a SAM to a hydrodynamical simulation, Short & Thomas (2009) showed that their hybrid feedback model could reproduce the observed mean L_X–T_X relation for groups and poor clusters at $z = 0$, but only if there was a large energy input into the ICM from AGN over the entire formation history of haloes. The AGN heating is efficient at driving X-ray emitting gas from the central regions of low-mass haloes, reducing their luminosity and steepening the L_X–T_X relation as desired. Unlike the simple pre-heating scenario, their model was also able to account for some of the scatter about the mean relation seen for temperatures $T \lesssim 3$ keV, attributable to the varied merger histories of groups. In addition, the gas fractions of their simulated groups and poor clusters were found to broadly agree with observational data, rapidly declining at low temperatures and exhibiting a comparable amount of scatter.

The main limitation of both the PC and the FO simulations is that neither can reproduce the low entropy found in the centres of cool-core (CC) clusters. For the FO run this is because cooling is not incorporated in the hydrodynamical simulations, whereas in the PC run pre-heating expels gas from cluster cores at high redshift, limiting the subsequent cooling.

The cosmological model adopted in all three Millennium Gas simulations is a spatially flat ΛCDM model with parameters $\Omega_{m,0} = 0.25$, $\Omega_{b,0} = 0.045$, $\Omega_{\Lambda,0} = 0.75$, $h = 0.73$, $n_s = 1$ and $\sigma_{8,0} = 0.9$. Here $\Omega_{m,0}$, $\Omega_{b,0}$ and $\Omega_{\Lambda,0}$ are the total matter, baryon and dark energy density parameters, respectively, h is the Hubble parameter in units of $100\,\mathrm{km\,s^{-1}\,Mpc^{-1}}$, n_s is the spectral index of primordial density perturbations and $\sigma_{8,0}$ is the rms linear density fluctuation within a sphere of radius $8\,h^{-1}$ Mpc. The subscript 0 signifies the value of a quantity at the present day. These cosmological parameters are the same as those used in the original millennium simulation and are consistent with a combined analysis of the first-year *Wilkinson Microwave Anisotropy Probe* (*WMAP*) data (Spergel et al. 2003) and data from the Two-degree-Field Galaxy Redshift Survey (Colless et al. 2001). However, there is some tension between the chosen parameter values, particularly n_s and $\sigma_{8,0}$, and those derived from the 7-yr *WMAP* data (Komatsu et al. 2010). More significantly

for this paper, the mean value of the baryon density, $f_b = 0.18$, is higher than the *WMAP* 7-yr value of $f_b = 0.167$.

2.2 Cluster catalogues

Cluster catalogues are generated at several redshifts for the three Millennium Gas simulations using a procedure similar to that employed by Muanwong et al. (2002). Essentially, a friend-of-friends algorithm is used to identify peaks in the density field and then spheres are grown around these peaks until they enclose regions of a given overdensity.

We define overdensity, Δ, with respect to the critical density, ρ_c, at any given redshift:

$$\Delta = \frac{\bar{\rho}(<r)}{\rho_c} = \frac{2GM(<r)}{r^3H^2}, \quad (1)$$

where $\bar{\rho}$ is the mean density within radius r, M is the mass within this region and G is the gravitational constant. We express our masses in units of $h^{-1}\,\mathrm{M}_\odot$, rescaling observational data to this system when required.

Low-mass clusters are more affected by non-gravitational heating processes than high-mass ones. Observationally, temperature is often used as a proxy for mass as the two are strongly correlated. For that reason, we often divide the clusters into bins according to their spectroscopic-like temperature, T_{sl}, defined as

$$T_{sl} = \frac{\int \rho^2 T^{1/4}\,\mathrm{d}V}{\int \rho^2 T^{-(3/4)}\,\mathrm{d}V}, \quad (2)$$

where ρ is the gas density, T the physical temperature and the integral runs over volume. Mazzotta et al. (2004) have shown T_{sl} to be a good approximation to the temperature recovered by X-ray spectral analysis software in the bremsstrahlung regime.

The scaling relations for the GO and PC runs can be dominated by small objects. For this reason, we remove many clusters from our sample such that the remaining clusters are distributed evenly in $\log(M_{200})$, with a lower mass limit $M_{2500} > 1.73 \times 10^{13}\,h^{-1}\,\mathrm{M}_\odot$ that corresponds to 1000 particles each of gas and dark matter within R_{2500}. For the FO run, we resimulate all clusters with $kT_{sl} > 3$ keV and a selection of clusters below this temperature, again chosen evenly in $\log(M_{200})$. This has a much higher mass resolution and so the lower mass limit in this case, $M_{200} > 1.2 \times 10^{13}\,h^{-1}\,\mathrm{M}_\odot$, was instead fixed by the total number of clusters that we wish to simulate. When plotting as a function of mass at an overdensity other than the one used in the selection procedure, there will not be a clean lower mass limit; however this is a very minor effect that does not lead to any significant bias in our results.

3 RESULTS

In this section we first discuss the radial profiles of the hot gas fractions of clusters at the present day. We then characterize the dependence of the hot gas fraction upon cluster mass, and investigate the scatter about that mean relation. Finally, we look at the variation of the hot gas fraction with redshift.

3.1 Profiles

3.1.1 Differential hot gas profiles

Fig. 1 shows the differential gas mass fraction profiles for clusters in three temperature ranges, $kT_{sl} > 5$ keV (upper, green regions), $2.5 < kT_{sl} < 5$ keV (middle, cyan regions) and $kT_{sl} < 2.5$ keV (lower, magenta regions). The curves are plotted out to beyond r_{500} (the radius at which $\Delta = 500$), which is the region accessible to X-ray observations.

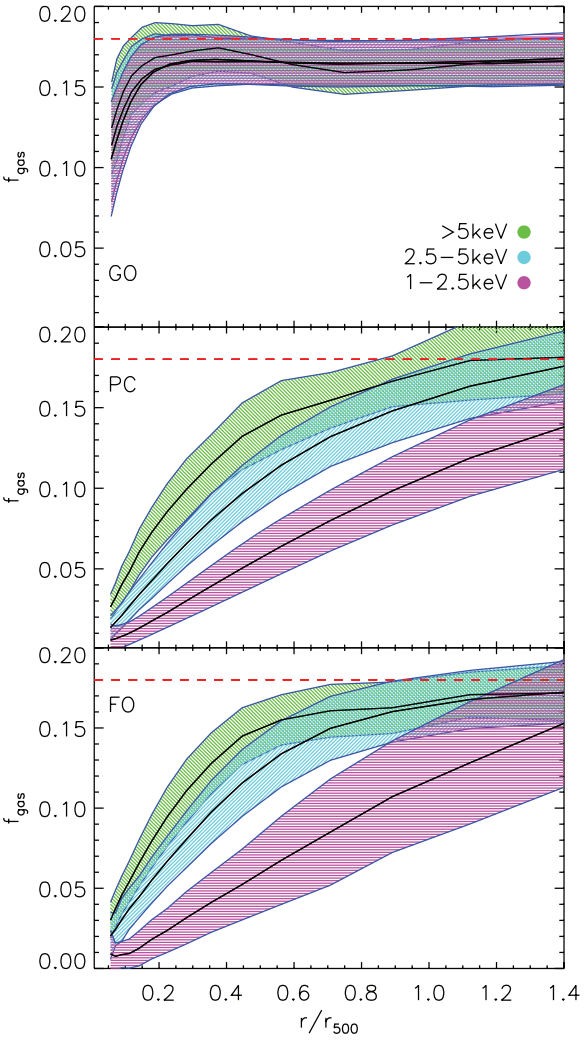

Figure 1. Differential hot gas fraction profiles. The solid lines show the mean relations and the shaded region the 1σ scatter. The upper, green regions correspond to clusters with spectroscopic-like temperatures above 5 keV; the middle, cyan regions to 2.5–5 keV and the lower, magenta regions to clusters in the range 1–2.5 keV. Profiles are only plotted for radii greater than the gravitational softening length. The dashed line in each case shows the cosmic mean.

For the GO run the gas fraction plateaus at a value of 0.16–0.17 at about $0.3\,r_{500}$, although there is a very slow increase at larger radii (beyond the right-hand edge of the plot). This is less than the global baryon fraction of 0.18: conversion of kinetic energy into heat, together with continual stirring of the gas by the motion of dark matter structures, allows the gas to pick up energy at the expense of the dark matter (e.g. Pearce, Thomas & Couchman 1994). This is particularly evident in the cluster cores: for the largest clusters, r_{500} is of order $1\,h^{-1}$ Mpc; therefore the drop in baryon fraction in the core of the clusters occurs on a scale significantly larger than the force softening ($25\,h^{-1}$ kpc).

In the PC and FO runs, gas has been expelled from the cluster cores and pushed to larger radii. The effect is more pronounced at lower masses: thus the gas profiles of clusters with $kT_{sl} < 2.5$ keV are still steeply rising at r_{500}, while for $kT_{sl} > 5$ keV the profiles are

approximately constant beyond this radius. The inconstancy of the gas fraction is both a nuisance, requiring careful calibration before we can use clusters as cosmological probes, and a useful test of any model of entropy generation in the ICM.

3.1.2 Comparison with observations

Rather than plotting differential profiles, observational studies tend to report the cumulative gas fractions, averaged within some radius. Fig. 2 shows the cumulative gas fraction profiles in the FO run compared to several different observational studies (Vikhlinin et al. 2006; Allen et al. 2008; Pratt et al. 2010). We have only plotted simulated clusters in temperature ranges corresponding to those of the various observational data sets. To save space, we do not show the results from the PC run – these are similar.

All three observational studies plot the gas fractions using a different ordinate. The top panel, from Vikhlinin et al. (2006), uses overdensity relative to the critical density. They looked at 13 *Chandra* clusters with a range of temperatures upwards of about 1.5 keV for which the data extend out to large radii. The simulated and observed clusters agree at the outer limit of the data, but the former fall more rapidly as one moves into the cluster centre.

The middle panel shows data from Allen et al. (2008). They again study *Chandra* clusters, but they focus on the inner regions of 42 hot ($kT_{\rm sl} > 5$ keV) systems. As can clearly be seen, the simulated clusters lie well below the observations within r_{2500}.

Both the above studies focus on bright, relaxed systems (those that are likely to be labelled CC). By way of contrast, the REXCESS survey (Böhringer et al. 2007; Pratt et al. 2010), shown in the lower panel of Fig. 2, is a sample of 33 nearby galaxy clusters from *XMM–Newton*, selected so as to sample a broad range of luminosities and with no bias towards any morphological type. The temperature range here is 2–9 keV with the more massive clusters lying towards the upper edge of the observed band, and the least massive ones towards the bottom. Here the simulations are much more successful in reproducing the observed profiles, providing a fair match to the non-cool-core (NCC) population out to the limit of the observations. They fail to reproduce CC clusters (those with flattened baryon fraction profiles in their inner regions), however these are much less frequent than in the relaxed samples.

We conclude that our simulated clusters provide a fair match to the hot gas fractions in typical NCC clusters, but fail to reproduce the higher gas fractions seen in the central regions of the brighter, CC clusters.

The results for our adiabatic haloes agree with other previous simulations undertaken with smoothed particle hydrodynamics (e.g. Kravtsov, Nagai & Vikhlinin 2005; Ettori et al. 2006; Crain et al. 2007). Direct comparison of the other runs is more difficult because we use different feedback models.

Qualitatively, we see a similar behaviour in the profiles of the hot gas fraction to previous work, but the baryon fraction profile is very different in our FO run because of the much reduced stellar fraction. The integrated baryon fractions within r_{500} are considered in Section 3.2.3.

3.2 Scaling relations

3.2.1 Cumulative hot gas fractions

Fig. 3 shows the cumulative gas fraction within a radius of r_{500} as a function of total mass. The GO points are consistent with a constant value of 0.162, slightly smaller than the universal mean of 0.18. By

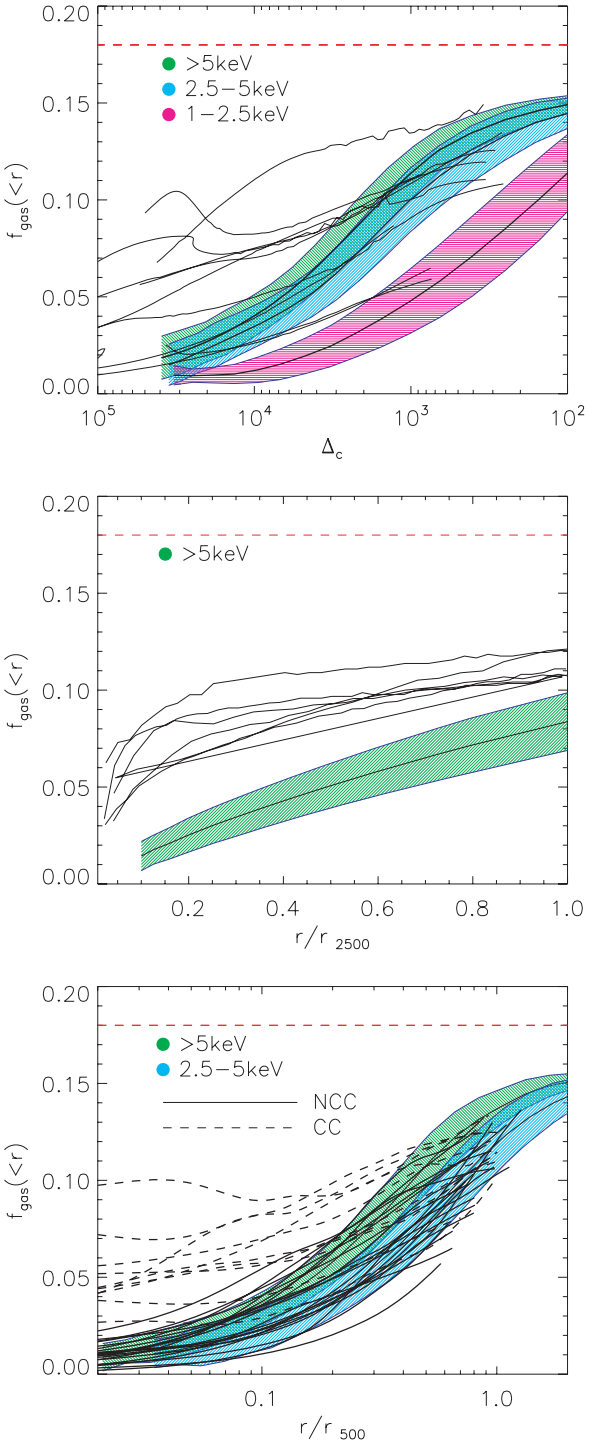

Figure 2. Comparison of the cumulative hot gas fraction profiles in the FO run with those of Vikhlinin et al. (2006, upper panel), Allen et al. (2008, middle panel) and Pratt et al. (2010, lower panel). In each case the coloured bands refer to the 1σ spread of profiles seen in the simulations: upper, green ($kT_{\rm sl} > 5$ keV); middle, cyan ($2.5 < kT_{\rm sl} < 5$ keV); lower, magenta ($1 < kT_{\rm sl} < 2.5$ keV). The profiles of simulated clusters are only plotted for radii greater than the softening length. The observational data are shown by black lines, in the lower panel, with solid and dashed lines corresponding to NCC and CC clusters, respectively.

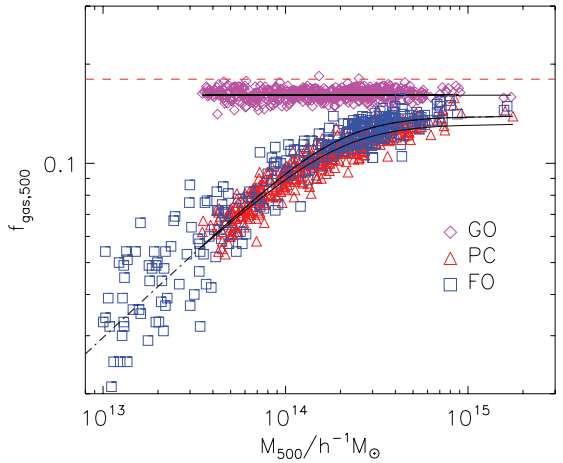

Figure 3. The cumulative hot gas fraction within r_{500} as a function of total mass. The solid lines show the best-fitting mean relations, as described in the text and Table 1. Extending the fit to the whole range of the FO data, as shown by the dot–dashed line, makes almost no difference to the fit. The dashed line shows the mean baryon fraction in the simulation.

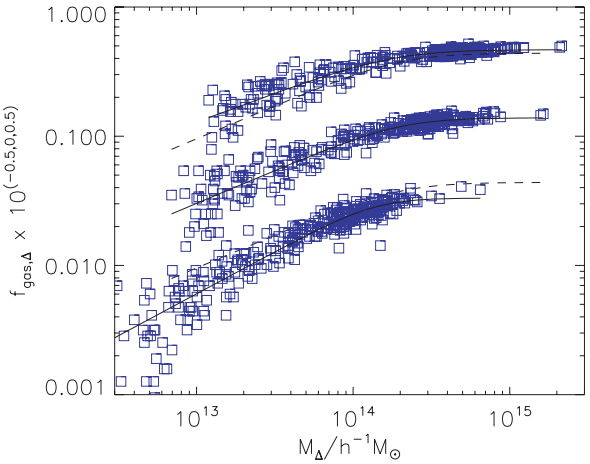

Figure 4. The baryon fraction within three different radii for the FO run: r_{200} (upper), r_{500} (middle) and r_{2500} (lower). For clarity, the upper and lower data points have been shifted by 0.5 dex. The solid lines show the best-fitting mean relations and the dashed lines the best-fitting mean relation for the r_{500} data.

contrast, both the PC and the FO runs have hot gas fractions that are strong functions of mass, because the feedback processes are more effective in lower mass clusters and evacuate more of the gas.

Fig. 4 contrasts the hot gas fractions for the FO run within three different radii corresponding to enclosed overdensities of $\Delta = 200$, 500 and 2500 (the PC run gives similar results). In each case the mass has been measured within the corresponding radius. As expected from the radial profiles, the gas fraction is an increasing function of scale radius (i.e. decreasing overdensity). Note that, for a fixed enclosed mass, the variation in enclosed gas fraction is relatively modest: for example, at $M_\Delta = 10^{14}\,h^{-1}\,\mathrm{M}_\odot$ it varies from 0.07 for $\Delta = 2500$ to 0.10 for $\Delta = 200$. This is much less than the variation seen if a fixed overdensity is used to measure the mass, e.g. for $M_{500} = 10^{14}\,h^{-1}\,\mathrm{M}_\odot$, the enclosed gas fraction increases from 0.04 to 0.11 as the overdensity drops from 2500 to 200.

Table 1. Model parameter fits to the hot gas fractions as a function of mass, as described by equation (3) with a fixed value of $\zeta = 4$. Here $m = \log_{10}(M_0)$. Typical 1σ errors in f_0, m and s are 0.005, 0.2 and 0.04, respectively. For the GO run, there is no discernible mass-dependence in the hot gas fractions and so only the mean value is recorded in column f_0. The final column gives the rms scatter in dex of the data points about the best-fitting line.

Model	Overdensity	f_0	m	s	σ
GO	2500	0.158			0.036
	500	0.161			0.018
	200	0.163			0.013
	500\2500	0.164			0.026
	200\500	0.166			0.033
PC	2500	0.103	14.15	0.590	0.048
	500	0.134	14.26	0.519	0.041
	200	0.150	14.43	0.363	0.027
	500\2500	0.161	14.28	0.393	0.037
	200\500	0.180	14.10	0.263	0.044
FO	2500	0.126	14.25	0.650	0.124
	500	0.143	14.26	0.552	0.061
	200	0.148	14.21	0.472	0.058
	500\2500	0.163	14.13	0.492	0.076
	200\500	0.173	13.72	0.512	0.066

In Figs 3 and 4, we fit the hot gas fraction scaling relations with models of the form:

$$\log_{10} f = \log_{10} f_0 + s(\mu - \log[1 + \exp(\zeta\mu)]/\zeta), \quad (3)$$

where $\mu = \log_{10}(M/M_0)$ and f_0, M_0, ζ and s are fitting parameters. In log space, this represents a line of constant slope, s, at masses well below M_0, bending over to a constant value of f_0 at high masses. For low enclosed overdensities, we would expect f_0 to tend towards the universal baryon fraction of 0.18, although we do not impose this as a constraint. ζ is a parameter that controls the abruptness of the transition between the two regimes. The data are not always sufficient to independently constrain all the parameters, and in particular ζ: for that reason we use a fixed value of ζ when recording our fits. The best-fitting models are shown as solid lines in the figures, and the parameters are listed in Table 1, along with the scatter about the best-fitting relation.

Fig. 5 shows the cumulative hot gas fractions in the FO run within r_{2500} and r_{500} as a function of mass. The shaded region shows the 1σ spread about the mean relation from the simulation and the points are observational data from the sources listed in the figure caption. Concentrating first on the upper panel, it is apparent that there are systematic differences in the reported hot gas fractions that cannot be attributed solely to statistical error. In particular, the Allen et al. (2008) data lie significantly above those of the other studies. This may be because they concentrated on regular, CC clusters that are likely to lie up the upper edge of the distribution. Even given these observational inconsistencies, however, the simulations show a much greater variation in gas fraction with M_{2500} than do the observations. It would seem that in the FO run (and the PC run is similar) we have ejected too much material from within this radius in small clusters, and too little in large ones.

Moving out to r_{500}, as shown in the lower panel of the figure, the simulations and observations are in better agreement. There is again a suggestion that the observational data would prefer higher gas fractions than the simulations below a cluster mass of $5 \times 10^{13}\,h^{-1}\,\mathrm{M}_\odot$, but the scatter in the observational measurements is large. At higher masses, the two show a similar trend of increasing gas fraction with cluster mass, although the simulated values are

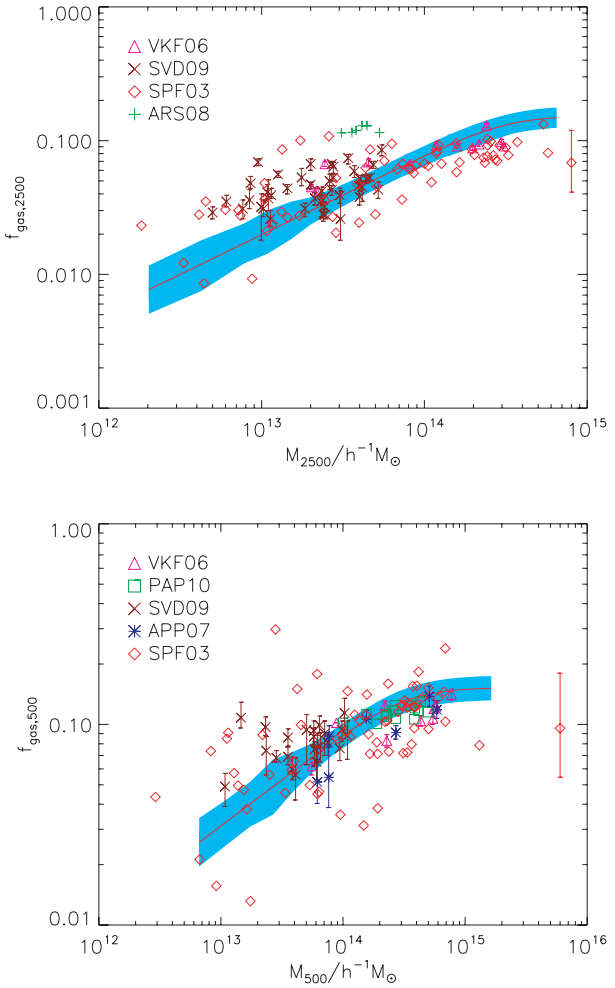

Figure 5. The cumulative hot gas fraction versus mass relations for the FO run as compared to observations. The upper and lower panels refer to overdensities of 2500 and 500, respectively. The shaded regions are the 1σ spread in the simulated clusters. The symbols represent observational data from Sanderson et al. (2003), Vikhlinin et al. (2006), Arnaud, Pointecouteau & Pratt (2007), Allen et al. (2008), Sun et al. (2009) and Pratt et al. (2010). For the Sanderson et al. (2003) clusters, we show one fake data point on the right-hand edge of the plots with typical 1σ (statistical) error bars. For the other samples, we include the error bars on the plotted points, apart from Allen et al. (2008) and Pratt et al. (2010) since we do not know the uncertainties in their measurements.

perhaps slightly too high. This is presumably because the mean baryon fraction that we have used in the simulations, 0.18, is higher than the current *WMAP* best-fitting value of 0.168.

3.2.2 *Differential hot gas fractions*

The profiles of Fig. 1 suggest that the differential gas fraction between radii of r_{2500} and r_{500} may provide a measure that is more independent of mass than the cumulative gas fractions of the previous section.

In Fig. 6 we show differential gas fractions, $r_{2500} - r_{500}$ and $r_{500} - r_{200}$, for the FO model (once again, the PC run gives similar results). Both are higher than the equivalent cumulative measures, although the universal gas fraction is reached only for the most massive clusters ($M_{200} > 3 \times 10^{14}\,h^{-1}\,\mathrm{M}_\odot$) at radii $r > r_{500}$. Clearly the differential gas fraction at larger radii, $r_{500} - r_{200}$, is more

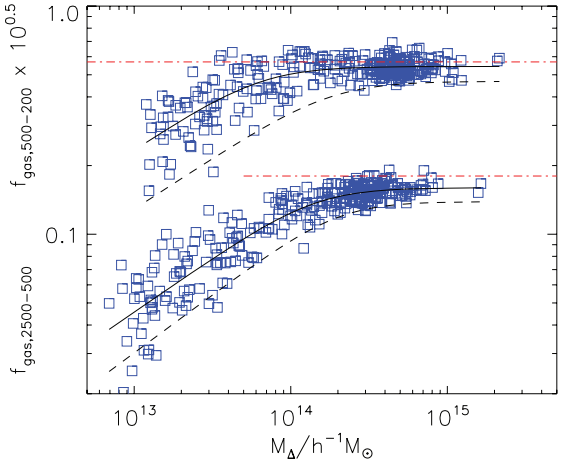

Figure 6. Differential hot gas fractions for the FO runs: between r_{2500} and r_{500} (lower points) and between r_{500} and r_{200} (upper points). The upper points have been shifted up by 0.5 dex, for clarity. In each case, the mass has been taken to be that at the outer edge of the differential range. The solid lines show the best-fitting mean relation and the dashed lines show the best-fitting relation for the equivalent cumulative gas fraction measure. The dot–dashed lines show the mean baryon fraction in the simulation.

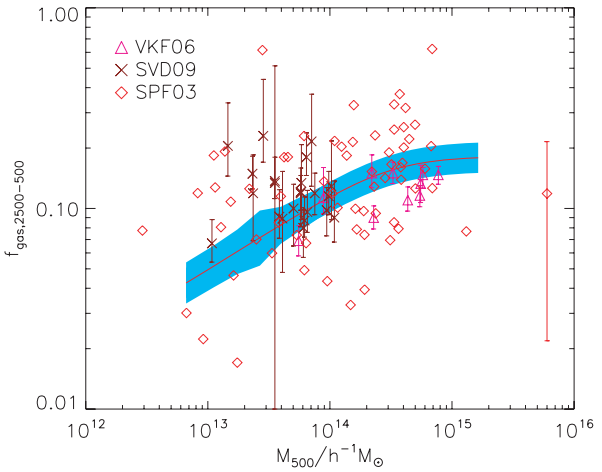

Figure 7. The differential hot gas fraction in the annulus contained between r_{2500} and r_{500} for the FO run as compared to observations. The shaded region is the 1σ spread in the simulated clusters. The points are taken from Sanderson et al. (2003), Vikhlinin et al. (2006) and Sun et al. (2009). For the Sanderson et al. (2003) clusters, we show one fake data point on the right-hand edge of the plot with typical 1σ (statistical) error bars. For the other samples, we draw the error bars on the plotted points.

nearly constant and so provides the more accurate probe of cosmology, but observationally the inner annulus, $r_{2500} - r_{500}$, provides a compromise between eliminating the depleted inner region and having enough counts to enable a reliable X-ray determination of the gas density. The observational data from Sanderson et al. (2003), Vikhlinin et al. (2006) and Sun et al. (2009), plotted in Fig. 7, present a confused picture. The Sanderson et al. (2003) data broadly mimic the simulations, but the statistical scatter in their data is very large. Vikhlinin et al. (2006) report the smallest error bars for their data and find differential gas fractions that increase strongly with mass, but which lie below the simulated values; whereas, at lower masses, the Sun et al. (2009) data seem to require hot gas fractions that are decreasing, or at best flat, as a function of mass. We conclude that

Table 2. As for Table 1 but for the baryon fractions rather than the hot gas fractions. ζ = is fixed at 4 for the PC and 8 for the FO run. For the GO run there is no star formation and so the values are the same as reported in Table 1.

Model	Overdensity	f_0	m	s	σ
PC	2500	0.141	14.32	0.250	0.061
	500	0.161	14.44	0.307	0.037
	200	0.168	14.49	0.271	0.030
	500\2500	0.174	14.29	0.362	0.035
	200\500	0.188	14.10	0.269	0.042
FO	2500	0.156	14.92	0.251	0.069
	500	0.150	14.48	0.308	0.052
	200	0.157	14.41	0.291	0.044
	500\2500	0.167	14.25	0.357	0.053
	200\500	0.181	13.94	0.333	0.058

these differential measurements are not yet sufficiently robust to provide useful constraints.

It is interesting to note that both the PC and FO models have higher differential gas fractions at large radii than does the GO model. The injection of entropy has removed gas from the cores of the clusters and pushed it out to larger radii, between r_{500} and r_{200}. In a steady state, the higher entropy in these runs would ensure that they have a lower gas density than in the GO model: we conclude that on large scales, although still within the virial radius, the clusters are not in dynamical equilibrium.

3.2.3 *Baryon fractions*

The baryon fractions are also well fit by the model given in equation (3) with parameters as listed in Table 2. Because clusters are large systems with deep potential wells, it is often stated that they should enclose a representative sample of the Universe, and in particular that they should contain the universal fraction of baryons. Indeed, we find this is approximately true, with only a small baryon deficit within r_{200}.

Observationally, the baryon fraction is hard to determine because of the difficulty in measuring the contribution from dwarf galaxies and from intracluster light (stars that have been stripped from galaxies). This latter component may comprise as much as 40 per cent of the total light of the cluster (Bernstein et al. 1995; Gonzalez et al. 2000; Feldmeier et al. 2002, 2004; Gonzalez, Zabludoff & Zaritsky 2005; Zibetti et al. 2005; Krick, Bernstein & Pimbblet 2006). Except for the brightest X-ray clusters, the measurement of total mass is also problematic.

Gonzalez, Zaritsky & Zabludoff (2007, hereafter GZZ07), in a sample of 12 groups and clusters spanning a wide mass range, find that the baryon fraction is independent of mass and averages to 0.133 within r_{500}. Laganá et al. (2008, hereafter LLA08) with a smaller sample of five high-mass clusters find a slightly lower value of 0.123 (the mean of their quoted numbers, weighted by the inverse square of their errors). On the other hand, Giodini et al. (2009, hereafter GPF09), in a sample of 41 clusters drawn from Vikhlinin et al. (2006), Arnaud et al. (2007) and Sun et al. (2009) find that the baryon fraction is a slowly increasing function of mass. The baryon fractions for our FO and PC clusters are compared to these observations in Fig. 8.

The observations and the simulations approximately agree for cluster masses of 1–3 $\times$ $10^{14}\,h^{-1}$ $M_\odot$. However, the simulations show a strong variation with cluster mass, even more so than that of

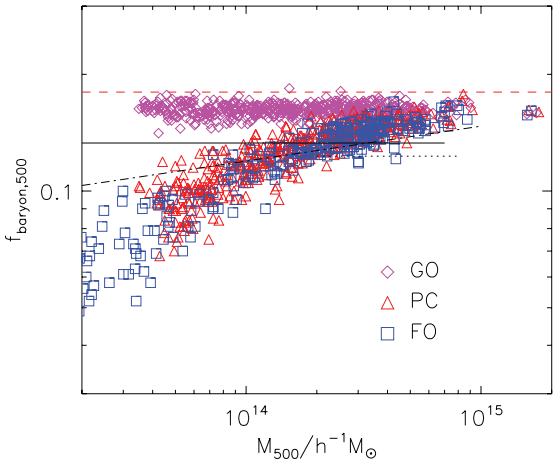

Figure 8. The cumulative baryon fraction versus mass. The solid and dotted lines show the mean relations (approximately independent of mass) from Gonzalez et al. (2007) and Laganá et al. (2008), respectively; the dot–dashed line shows that from Giodini et al. (2009). The red dashed line is the universal mean.

GPF09. This difference is attributable mainly to differences in star formation, as described below.

3.2.4 *Stellar fractions*

Both our PC and FO models have much more modest star formation than do many previous simulations (e.g. Borgani et al. 2004; Ettori et al. 2006; Kay et al. 2007a; Nagai, Kravtsov & Vikhlinin 2007; Davé, Oppenheimer & Sivanandam 2008; Fabjan et al. 2010; Puchwein et al. 2010). In particular, the FO run takes its star formation rate from the highly successful L-Galaxies SAM. The mean stellar fraction in our high-mass clusters in the FO run agrees well with the observations of both GZZ07 and LLA08; the results of GPF09 are slightly higher. However, we do not find such a strong increase in stellar fraction in low-mass clusters as is seen in both GZZ07 and GPF09. The upper panel in Fig. 9 shows the stellar mass fraction within r_{500} as a function of mass for both the PC and the FO runs, with the trend from GZZ07 shown as a solid line and that from GPF09 as a dotted line. This comparison suggests that we considerably underestimate star formation in groups. The lower panel shows a similar plot for r_{200} with data from Andreon (2010). He finds lower stellar fractions but a similar steep increase with decreasing mass.

Before dismissing our FO model as unrealistic, however, we note the following.

(i) As pointed out by Balogh et al. (2008), the GZZ07 data are incompatible with any model that forms galaxies via hierarchical mergers unless there is an unreasonably large star formation rate in groups at late times.

(ii) The L-Galaxies model produces correlation functions for the galaxy distribution that are consistent with observations with no evidence for a suppression at small separations (Kitzbichler & White 2008). It is difficult to reconcile this with the need to greatly increase the stellar fraction in groups.

The other simulations mentioned above also predict a slow variation of stellar fraction with mass, although they mostly have stellar fractions that are higher than ours, agreeing with the observations on group scales but having stellar fractions that are too high on cluster scales. For example, the clusters of Ettori et al. (2006) have

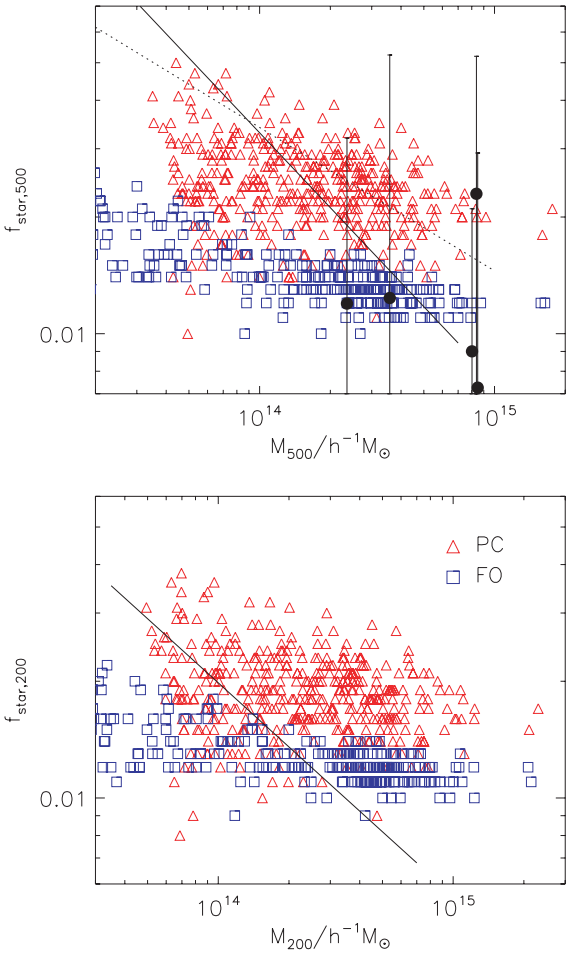

Figure 9. The cumulative stellar fraction versus mass. The upper panel shows the stellar fractions within r_{500}; the black dots are observed clusters from LLA08, the solid line shows the observed relation from GZZ07 and the dotted line that from GPF09. The lower panel is the stellar fraction within r_{200}, with the solid line showing the observed relation from Andreon (2010).

a stellar fraction of about 0.05 within r_{500}. The equivalent fraction for massive clusters ($kT_{\rm sl} > 5$ keV) in our own runs is 0.02 for PC and 0.013 for FO.[1]

We conclude that, although the observations are not yet sufficiently robust, stellar mass fractions provide an important test of, and discriminant between, different galaxy formation models.

3.2.5 Scatter in the scaling relations

In this section, we investigate why some clusters have slightly more hot gas, and others slightly less, than other clusters of the same mass. Our purpose in doing this is two-fold: first, to understand the physical reason for this scatter, and secondly to suggest corrections that can be applied to the observations to better allow gas fraction to be used as a probe of cosmology.

First note that, as is evident from Fig. 3, the mean gas fractions in the GO run are independent of mass. However, there is scatter

[1] Ettori et al. (2006) choose to give stellar fractions in terms of the mean baryon fraction, $Y = M_{\rm star}/M_{\rm total}/f_{\rm b}$. The stellar fractions quoted in their paper are thus a factor of 5.6 larger than those listed here.

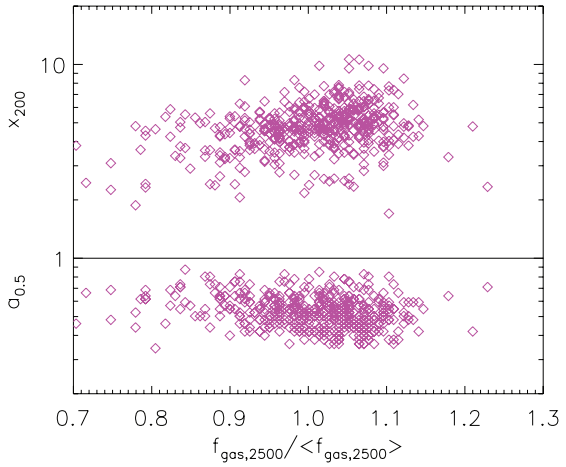

Figure 10. The strongest correlations of the scatter in the mean gas fraction within r_{2500} for the GO run. The upper points show the cluster concentration, and the lower points the expansion factor of the Universe at the time that the cluster had accumulated half its final mass.

about the mean gas fraction that we might hope to relate somehow to the physical properties of the cluster.

We have checked for correlations of the scatter with every conceivable physical quantity (including substructure, merging history, angular momentum, etc.) and find many weak correlations, but no strong one. Fig. 10 shows a positive correlation with concentration, i.e. more concentrated clusters have a greater gas fraction than the average within r_{2500}. Likewise, clusters that form earlier have a greater gas fraction than those that form later. The correlation coefficients for these two relations are 0.29 and −0.23, respectively. These may be two aspects of the same relation as concentration shows a negative correlation with formation time. The appendix describes how we measure each of these for the clusters in our simulation. Both are correlated with cluster mass, but it turns out that they are more strongly correlated with each other.

The physical mechanism that may drive the correlations seen in Fig. 10 is unclear: it primarily affects the core of the cluster as the correlations get weaker if one measures the gas fraction within larger radii. It may be that the degree of gravitational pre-heating is greater in systems that form later (see e.g. Mo et al. 2005).

Other quantities that we have tested include the halo angular momentum, merger history and substructure. Once the primary correlation of gas fraction with mass is removed, none of these shows any correlation with the residual gas fraction.

Observationally, of course, an excess core gas fraction is associated with an increase in X-ray luminosity. Thus, as shown in Fig. 11, the excess luminosity of a cluster above the mean $L_{\rm X}$–$T_{\rm sl}$ relation is correlated with the presence of excess gas in the cluster. The correlation coefficients in this case are 0.51 and 0.73 for the PC and FO run, respectively. A similar result was found for the PC run by Stanek et al. (2010). This correlation may serve to reduce the scatter from the major outliers in the gas fraction–mass relation.

3.3 Evolution

3.3.1 Profiles

Fig. 12 shows the evolution of the cumulative gas fraction profiles of the 10 most massive clusters, for each of the runs.

Looking first at the GO run in the upper plot, it can be seen that the gas fraction within r_{500} remains largely constant over time: this is

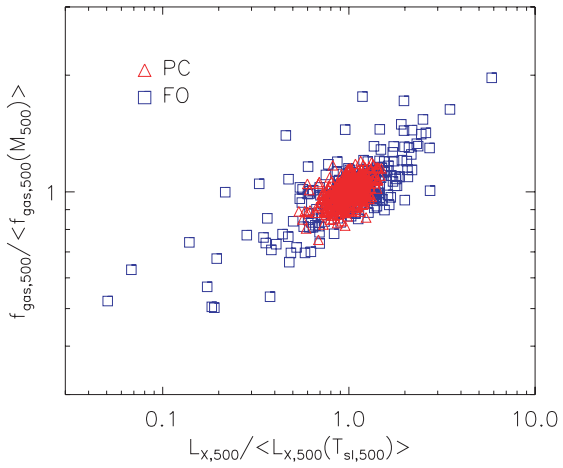

Figure 11. The deviation from the mean gas fraction–mass relation plotted against the deviation from the mean luminosity–temperature relation. Properties are measured within a radius of r_{500}. Shown are the ratio of the measured quantities compared to that of the best-fitting mean relation.

to be expected for self-similar evolution. As the effective resolution increases (i.e. the ratio of the smoothing length to r_{500} decreases) so the gas fraction within the cluster core can be seen to be depleted, though still much higher than in the other two runs.

In the PC simulation, the gas fractions at high redshift are much reduced over their current-day values. This is because a large amount of energy has been injected into the ICM at early times, expelling gas from the clusters. Subsequently, the gas falls back into the clusters as the Universe evolves and tends towards (but falls far short of) self-similar evolution. In other words, the early entropy injection becomes relatively less important in more massive systems at late times.

This is in contrast to the behaviour in the FO run. Here we have continual injection of energy so that gas fraction profiles remain constant over time. Although our simulation takes its level of feedback from an SAM, nevertheless it seems to have achieved a homologous evolution.

Thus, although the PC and FO clusters have indistinguishable gas profiles at the current day, they look very different in the past. This casts doubt on the use of the measured gas fraction as a cosmological probe, but instead opens the possibility that it can be used to determine the nature of the feedback mechanism: in particular, to distinguish between early (PC) and continual (FO) heating.

3.3.2 Scaling relations and comparison with observations

Fig. 13 shows the hot gas fractions within r_{500} at a redshift $z = 1$ for clusters in our three simulations. For comparison, we also plot high-redshift systems ($0.8 \leq z \leq 1.3$) from a catalogue of clusters observed with *Chandra* compiled by Maughan et al. (2008). Note that Maughan et al. (2008) do not themselves present $f_{\rm gas}$ values. To compute them, we first determine the total mass, M_{500}, from the supplied values of $Y_{\rm X}$ (where $Y_{\rm X}$ is defined as the product of the gas mass within r_{500} and the spectroscopic-like temperature in the spherical annulus $0.15\,r_{500} < r \leq r_{500}$) by using the $Y_{\rm X}$–M_{500} relation derived from the sample of Vikhlinin et al. (2006). This is the procedure adopted by Maughan et al. (2008, see their equation 4). The gas fraction then follows upon taking the ratio of the gas mass interior to r_{500} (tabulated in their paper) to the total mass. The errors on the observational data points in Fig. 13 are computed

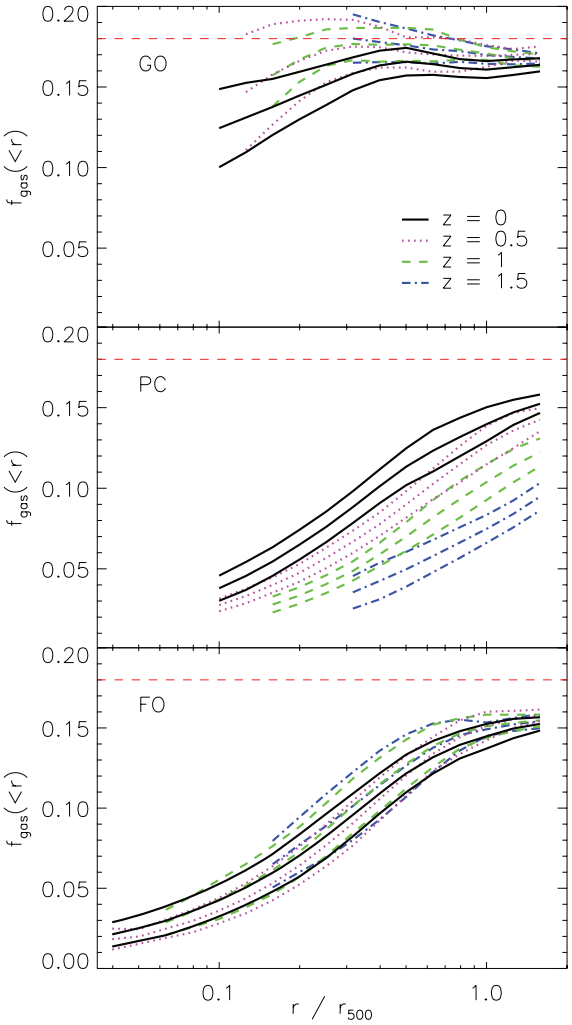

Figure 12. The evolution of the cumulative gas fraction profiles of the 10 most massive clusters. In each case, the dot–dashed blue, dashed green, dotted magenta and solid black lines correspond to $z = 1.5$, 1, 0.5 and 0, respectively. The middle line of each set is the mean of, and the upper and lower the 1σ spread in, the gas fraction profiles. The red dashed line is the universal mean.

using the supplied statistical errors on the gas mass and the core-excised temperatures. We compute errors on $f_{\rm gas}$ in this way, rather than using the errors on $Y_{\rm X}$, because the gas mass and temperature are independent measurements.

The different evolutionary behaviour of the gas fraction profiles is reflected in that of the mean gas fractions: the PC clusters have significantly smaller gas fractions at early times than those in the FO run. On the whole, the predictions of the FO model provide a closer match to the observational data than those of the PC model, but it seems as if some of the observed data points lie below the lower edge of the FO $f_{\rm gas}$–M_{500} relation. This could be because the mean cosmic baryon fraction in our simulations is higher than that measured by the *WMAP* satellite. If we were to repeat our simulations with the measured value of $f_{\rm b}$, we would expect all relations in Fig. 13 to be shifted downwards, improving the agreement between our FO model and the observations.

However, we note that the observational mass estimates may be lower than the true mass, because they are derived from a $Y_{\rm X}$–M_{500} relation that was calibrated using clusters with hydrostatic

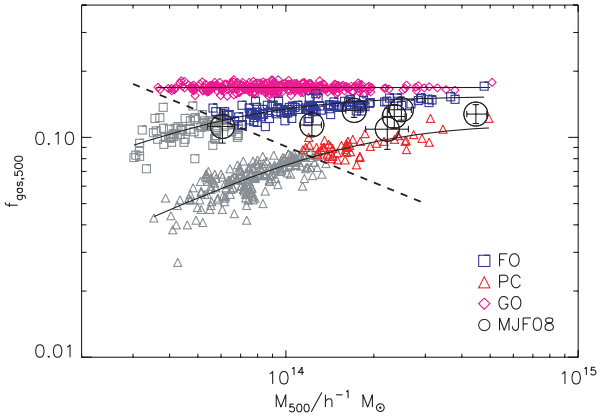

Figure 13. Gas fractions within r_{500} at $z = 1$ as a function of total mass. The solid lines show the best-fitting mean relations. The black circles are high-redshift clusters ($0.8 \leq z \leq 1.3$) from the observational data set of Maughan et al. (2008). The dashed line illustrates the effect of imposing a typical survey flux limit of 6.5×10^{-14} erg s^{-1} cm^{-2} at $z = 1$; only clusters to the right of this line would actually be observed by such a survey (the observed cluster slightly to the left of this line is at a lower redshift $z \approx 0.8$).

mass estimates. Simulations have shown that the assumption of hydrostatic equilibrium can bias such mass estimates low by ∼10–20 per cent (Rasia et al. 2006; Kay et al. 2007b; Nagai et al. 2007; Burns et al. 2008; Piffaretti & Valdarnini 2008; Meneghetti et al. 2009), because of additional pressure support provided by subsonic bulk motions in the ICM and/or non-thermal components. This would imply a small systematic overestimate of the gas fraction, so the observational data points in Fig. 13 should be shifted downwards and to the right. Another potential source of systematic error is that the masses of high-redshift clusters in the sample of Maughan et al. (2008) were determined by assuming self-similar evolution of the Y_X–M_{500} relation.

It is also important to consider the effect of source selection on our results. Observational cluster selection is based on X-ray flux, so may be biased towards systems with higher baryon fractions, particularly at high redshift. It is not possible to quantify this effect precisely using the archival sample of Maughan et al. (2008) since their selection function is unknown. A simple way of estimating the impact of selection effects on our findings is to ask the question: given a typical flux-limited survey, which of our simulated clusters would actually be observed? For illustrative purposes, we choose a flux limit of 6.5×10^{-14} erg s^{-1} cm^{-2}, equal to that of the WARPS survey (Horner et al. 2008) from which many of the objects in the Maughan et al. (2008) sample are drawn. The effect of imposing this flux limit at $z = 1$ is shown by the dashed line in Fig. 13; only objects to the right of this line would be observed by a WARPS-like survey. Note that one of the clusters from Maughan et al. (2008) lies slightly to the left of this line; this is because it is at a lower redshift, $z \approx 0.8$. The important point to note is that, for both the PC and FO runs, there is only a narrow mass range where the bias is significant, with most clusters in the two samples remaining unaffected. Even if we took a much higher flux limit, it would require greatly increased scatter about the PC f_{gas}–M_{500} relation for consistency with the observations, which is not intrinsic to the model.

The best-fitting parameters to the scaling relation of equation (3) are shown as a function of redshift in Fig. 14. In the case of the GO run, we fit only the mean value of the gas fraction, f_0, which is well determined. For the other two runs, the shaded regions show the 1σ allowed parameter range determined from Monte Carlo Markov

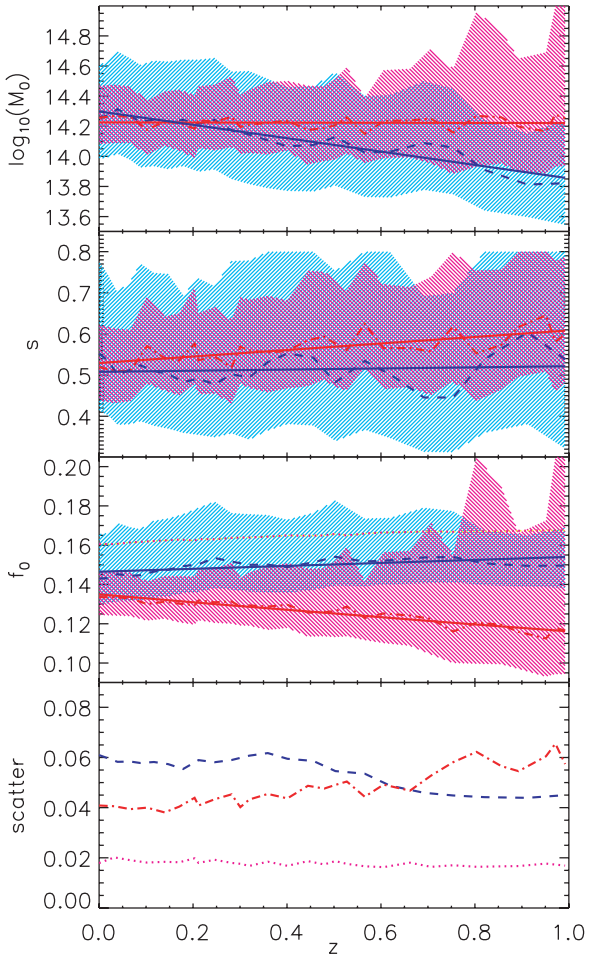

Figure 14. Evolution of the fitting parameters of equation (3) for the gas fraction within r_{500}: GO (dotted, magenta on yellow), PC (dot–dashed, red on magenta) and FO (dashed, blue on cyan) lines. The shaded region in each case shows the 1σ allowed parameter region. The lowest panel shows the rms scatter in dex about the best-fitting relation. The solid lines in the upper three panels show the best-fitting linear relations to the redshift evolution of the parameters.

Chain fitting. The parameters show considerable scatter, but this scatter is highly correlated. So while it is formally possible for both the PC and FO clusters to have the same value of f_0 at $z = 1$, for example, the other parameters must adjust themselves so as to maintain the difference in gas fraction seen in Fig. 13.

The solid lines in the upper three panels of Fig. 14 show straight-line fits to the evolution of each of the parameters with redshift – note that we fit to $\log_{10} f_0$ rather than f_0 as it is the former that appears in equation (3). These fits are listed in Table 3 and are used in the following section when comparing our model predictions with observations.

From the straight-line fits shown in Fig. 14, the mean gas fraction within r_{500} can be predicted for clusters of given mass and redshift using equation (3). This prediction is compared to observed gas fractions from the sample of Maughan et al. (2008) in Fig. 15. What is plotted here is the ratio of the observed gas fraction to the predicted one, so that perfect agreement would correspond to a value of unity, independent of redshift, but with some scatter due to the cluster-to-cluster variation and measurement error. The data are presented in this way since the gas fraction is a function of both cluster mass and redshift. The error bars are computed using

Table 3. Best-fitting straight lines to the evolution with redshift of the gas fraction model parameters shown in Fig. 14. These fits take the form $p = p_0 + s_p z$, where p is the parameter, p_0 its value at $z = 0$ and s_p the slope of the relation with redshift.

Parameter	Model	p_0	s_p
m	PC	14.23	0.00
	FO	14.30	−0.44
s	PC	0.53	0.08
	FO	0.51	0.01
$\log_{10} f_0$	PC	−0.870	−0.065
	FO	−0.834	0.022

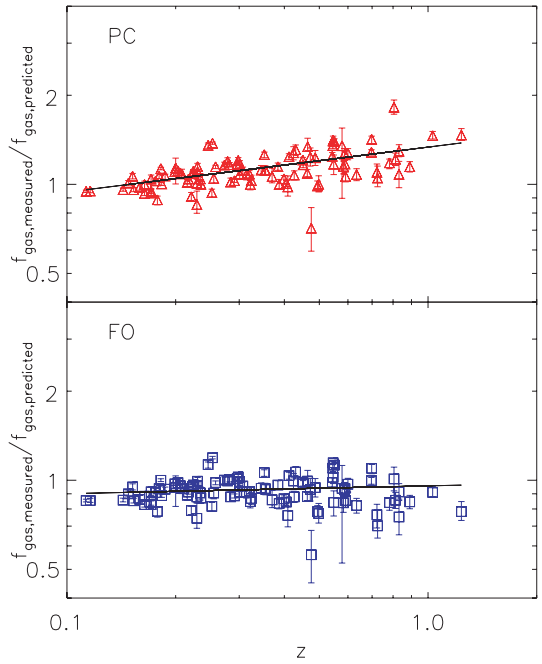

Figure 15. Ratios of the observed hot gas fractions within r_{500} from Maughan et al. (2008) to our model predictions. The solid lines show the best straight-line fits in $\log y$–$\log(1 + z)$ space.

Table 4. Best-fitting straight lines to the observed versus predicted hot gas ratios seen in Fig. 15 in linear and in $\log y$–$\log(1 + z)$ space. The allowed 1σ parameter ranges are calculated assuming that the expected variance about the best fit is equal to the observed one. The scatter is the rms scatter about the best-fitting line after allowing for the observational errors. In the log–log plots, the scatter is expressed in dex.

Model	Const.	Slope	Scatter
PC linear	0.960 ± 0.022	0.436 ± 0.064	0.074
log	0.126 ± 0.012	0.152 ± 0.020	0.028
FO linear	0.923 ± 0.019	0.002 ± 0.050	0.071
log	-0.019 ± 0.012	0.026 ± 0.020	0.034

the errors on the observed gas fractions (see above for details of how these were determined from the data of Maughan et al. 2008), accounting for the fact that the error on the total mass introduces an extra uncertainty when computing the theoretical prediction for the gas fraction.

It is immediately apparent that observations favour the FO prediction over the PC one, i.e. limited evolution in gas fraction since $z = 1$. This is shown in Table 4 where we list the allowable parameter ranges for straight line fits to the data, both in linear and in $\log y$–$\log(1 + z)$ space, where y is the ratio of observed to predicted gas fraction within r_{500}.

In making these fits, we treat the scatter about the mean relation as an unknown, $\sigma_{\rm scatter}$, independent of mass and redshift. The data are not good enough for a more sophisticated model, and that is likely, anyway, to make little difference to the fit. Given observational data, y_i, and errors, σ_i, we estimate the scatter as

$$\sigma^2_{\rm scatter} = \frac{\frac{1}{N-2}\sum_i \frac{(y_i - y_{i,\rm fit})^2}{\sigma_i^2} - 1}{\frac{1}{N}\sum_i \frac{1}{\sigma_i^2}}, \quad (4)$$

where $y_{i,\rm fit}$ are the best-fitting values. We iterate to convergence in $\sigma_{\rm scatter}$, at each stage minimizing the chi-squared statistic:

$$\chi^2 = \sum_i \frac{(y_i - y_{i,\rm fit})^2}{\sigma_i^2 + \sigma^2_{\rm scatter}}. \quad (5)$$

Note that the scatter about the best-fitting line is, in each case, lower than that seen in the simulations (as shown in the bottom panel of Fig. 14). Formally, therefore, neither of the models is a good fit. However, it seems unlikely that the true scatter in $f_{\rm gas}$ will be below that seen in the PC simulation. The uncertainty in the observed $f_{\rm gas}$ values is hard to determine, particularly at high redshift, so it is quite possible that the size of the error bars has been overestimated, leading to an underestimate of the intrinsic scatter.

For the PC simulation, the slope of the observed to simulated gas fraction ratio is incompatible with a horizontal line with high significance. The difference between the best-fitting values at $z = 0.1$ and 1 is about six times the scatter. Even if we were to account for observational bias in flux-limited samples towards clusters with higher baryon fractions, especially at high redshift, this is simply too large a difference to be explained by selection effects alone (recall our discussion of Fig. 13). We conclude that the PC model can be ruled out as a viable cause of entropy generation in the ICM.

The FO simulations, on the other hand, are perfectly consistent with a constant ratio of approximately unity. The slightly lower mean hot gas fraction for the observations as compared to the simulations can be explained by the fact that the latter have a higher mean baryon fraction than the *WMAP* 7-yr value.

We note that the analysis of Ettori et al. (2009) has many clusters in common with Maughan et al. (2008), but lists total masses and gas fractions that are often in disagreement. We are not certain why this is but note that there are differences in the analysis of the data, particularly in the cluster outskirts. We have repeated the analysis described in this section with the data of Ettori et al. (2009), but the data are much less constraining, principally because they quote much larger error bars. Nevertheless, one should bear in mind that systematic errors in the assumptions made in the data analysis could be degenerate with differences in the simulated ICM physics.

Looking at the problem in reverse, one could ask what errors could be introduced into the determination of cosmological parameters by the choice of an incorrect physical model for the evolution of the ICM. It is not possible to make a precise prediction for this using the current simulations as we only have access to a single realization with a particular set of cosmological parameters. Nevertheless, fixing the simulated clusters to be the same, Fig. 16 shows the effect of changing the observed cluster gas fractions in response to different values of Ω_Λ (fixing $\Omega_\Lambda + \Omega_{\rm m} = 1$). From this, it can be seen that using an incorrect physical model can have a dramatic effect, larger than that induced by changing cosmological parameters within any reasonable range.

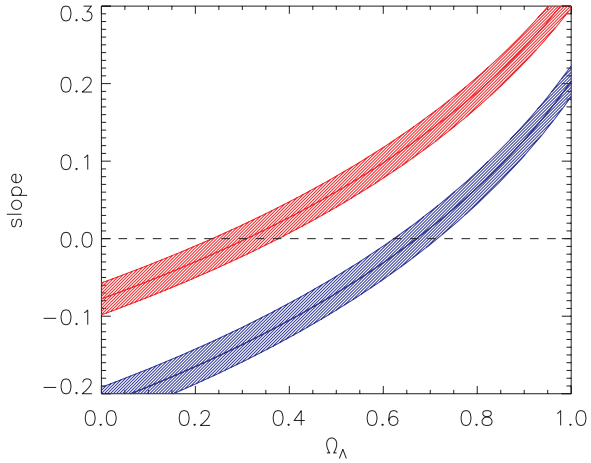

Figure 16. The relationship between the slope in log-space of the observed/simulated gas fraction ratio as a function of redshift and the value of Ω_Λ. The upper, red curve is for the PC run and the lower, blue curve for the FO run. The shaded regions show the formal 1σ confidence regions.

The analysis described in this section is necessarily very naive. A full treatment would require a detailed understanding of the selection function of observed clusters, modelling of the scatter in the scaling relations as a function of redshift and of the mean relations as a function of cosmological parameters. Nevertheless, none of this is likely to alter the basic conclusion that both observed clusters and those derived from our FO model show little evolution in hot gas fractions within r_{500} out to $z \approx 1$, whereas the PC model predicts a strong decline.

4 CONCLUSIONS

In this paper, we investigate the baryon content of clusters of galaxies in simulations using a variety of physical models for the ICM.

(i) GO – gravitational heating only with no radiative cooling. The purpose of this model is to test which aspects of the simulation evolve in a self-similar way and to provide a comparison for the other two runs.

(ii) PC – universal pre-heating to $200\,\mathrm{keV\,cm^2}$ at $z = 4$, plus radiative cooling and star formation. This represents widespread and early heating by objects that lie below the resolution limit of the simulation.

(iii) FO – feedback taken from an SAM, including heating from both SNe and AGNs, but without radiative cooling. The motivation for this model is to test heating from a realistic galaxy population that matches both the luminosity function and the black hole mass function of the current-day Universe.

The differential hot gas fraction profiles of clusters in the GO simulation are approximately constant at radii greater than $0.2r_{500}$, lying at 90 per cent of the cosmic mean. In the other two simulations, the profiles rise steeply from a low value in the cluster core before bending over to an approximately constant value at large radii; for the most massive clusters, $kT_{\rm sl} > 5\,\mathrm{keV}$, this occurs well within r_{500}.

The cumulative hot gas fraction profiles of our clusters in both the PC and FO runs lie well below those of the regular, CC clusters observed by Vikhlinin et al. (2006) and Allen et al. (2008). However, they provide a fair match to the NCC clusters found in the REXCESS representative cluster survey (Pratt et al. 2010).

When we look at integrated gas fractions within fixed radii, the agreement with observations is mixed. The total gas fraction within r_{2500} shows a stronger variation with cluster mass in the simulations than is seen in the observations. On the other hand, the agreement within r_{500} is much better, at least on scales above $5 \times 10^{14}\,h^{-1}\,\mathrm{M}_\odot$. There is a small offset but that can be explained by the fact that we adopt a mean baryon fraction in our simulations that is higher than the current best-fitting value from *WMAP*, respectively 0.18 and 0.168.

A more slowly varying function of mass is provided by the differential gas fraction between r_{2500} and r_{500}. Unfortunately, the scatter in the observational data is currently too large to allow any meaningful comparison with the simulations.

In agreement with previous work, our simulated clusters show a much smaller dependence of stellar fraction on mass than is seen in observations. Our stellar fractions within r_{500} are about 0.013 for massive clusters, $M_{500} > 10^{15}\,h^{-1}\,\mathrm{M}_\odot$, in the FO run, similar to observed values. The PC run gives slightly higher values, 0.02, whereas previous simulations can have stellar fractions as high as 0.05 (i.e. as much as a third of all the baryons within the cluster turned into stars). On the other hand, for lower mass clusters, $M_{500} \sim 5 \times 10^{13}\,h^{-1}\,\mathrm{M}_\odot$, our mean stellar fractions of 0.015 (FO) and 0.03 (PC) are much lower than the observed value of about 0.05. We note that there is some theoretical difficulty in understanding such a steep dependence of stellar fraction on cluster mass and that the observational determination of this mass fraction is difficult especially in low-mass systems. While this should prove a fruitful line of investigation in the future, it is probably too early to draw firm conclusions about the validity of the models.

We have fitted the gas fractions as a function of mass to relations of the form given by equation (3), with the results shown in Table 1. The scatter about these mean relations is lowest for the GO run and significantly larger for the PC, and especially the FO runs. Unfortunately, the observational data are too poor to provide an accurate measure.

For the GO run, we might expect that the scatter about the mean gas fraction–mass relations has a physical origin in the formation history of the clusters. Indeed, there is a weak correlation/anti-correlation of gas fraction with concentration/formation time (most strongly with the expansion factor at the time that the cluster had accumulated half its current mass). The strongest correlation that might be used observationally to correct for scatter in the gas fractions is that between deviation from the mean $L_{\rm X}$–$T_{\rm sl}$ relation and the excess gas fraction.

Although the gas fraction profiles are very similar for both the PC and FO runs at $z = 0$, their evolution is very different. In the former, gas is heated and expelled from the clusters at early times, so that the gas is depleted at high redshift and gradually falls back into the cluster over time. By contrast, the continual injection of energy in the FO run leads to evolution that is close to self-similar.

The evolution of halo gas fractions can therefore be used as a strong discriminant between models. We compare our simulated clusters with the compilation of *Chandra* clusters from Maughan et al. (2008). The observational data are fully consistent with the FO predictions and disagree with the evolution seen in the PC simulation with high significance. We need to be a little careful in interpreting these results as this is a highly biased sample that may well contain a disproportionate number of luminous clusters at high redshift. However, the scatter in gas fraction is sufficiently small that, even if we only observed those clusters with high baryon fractions at high redshift, the disagreement between the observations and the PC prediction would still be significant. We conclude that the observations favour continual heating, as in our FO model, over significant pre-heating at high redshift.

A corollary of the strong dependence of gas fraction evolution on the physics of entropy generation is that it becomes very difficult to use the gas fraction as a probe of cosmology. The differences caused by uncertain gas physics currently swamp those caused by reasonable changes in cosmological parameters. In the future, as both observational data for high-redshift clusters and models of the ICM improve, a joint analysis should be undertaken that considers variations in both cosmological parameters and cluster physics.

The main limitation to our present study is that the absence of cooling in our FO simulation leaves us unable to model CC clusters. Whilst that does not significantly affect the gas fractions when integrated out to r_{500}, it would be clearly desirable to also reproduce the full range of gas fraction profiles at smaller radii. We are working on ways to introduce cooling into the FO scheme without leading to excess production of cooled gas in CC clusters.

ACKNOWLEDGMENTS

This work was supported by the STFC (grant number ST/F002858/1, PhD studentship). We would like to thank Adrian Jenkins for supplying the code to generate the initial conditions. The simulations were carried out using the HPC facility at the University of Nottingham and the Virgo Consortium facilities at Durham. Analysis was undertaken on the Archimedes cluster at Sussex. We are grateful to Steve Allen, Stefano Andreon, Gabriel Pratt, Alistair Sanderson, Alexey Vikhlinin and especially Ben Maughan for supplying us with observational data and helping us with its interpretation. We would like to thank the referee for their constructive comments which have strengthened this paper.

REFERENCES

Allen S. W., Schmidt R. W., Fabian A. C., 2002, MNRAS, 334, L11
Allen S. W., Schmidt R. W., Ebeling H., Fabian A. C., van Speybroeck L., 2004, MNRAS, 353, 457
Allen S. W., Rapetti D. A., Schmidt R. W., Ebeling H., Morris R. G., Fabian A. C., 2008, MNRAS, 383, 879
Andreon S., 2010, MNRAS, 407, 263
Arnaud M., Pointecouteau E., Pratt G. W., 2007, A&A, 474, L37
Ascasibar Y., Sevilla R., Yepes G., Müller V., Gottlöber S., 2006, MNRAS, 371, 193
Balogh M. L., McCarthy I. G., Bower R. G., Eke V. R., 2008, MNRAS, 385, 1003
Bernstein G. M., Nichol R. C., Tyson J. A., Ulmer M. P., Wittman D., 1995, AJ, 110, 1507
Bialek J. J., Evrard A. E., Mohr J. J., 2001, ApJ, 555, 597
Böhringer H. et al., 2007, A&A, 469, 363
Borgani S., Governato F., Wadsley J., Menci N., Tozzi P., Quinn T., Stadel J., Lake G., 2002, MNRAS, 336, 409
Borgani S. et al., 2004, MNRAS, 348, 1078
Borgani S., Finoguenov A., Kay S. T., Ponman T. J., Springel V., Tozzi P., Voit G. M., 2005, MNRAS, 361, 233
Brighenti F., Mathews W. G., 2001, ApJ, 553, 103
Burns J. O., Hallman E. J., Gantner B., Motl P. M., Norman M. L., 2008, ApJ, 675, 1125
Colless M. et al., 2001, MNRAS, 328, 1039
Crain R. A., Eke V. R., Frenk C. S., Jenkins A., McCarthy I. G., Navarro J. F., Pearce F. R., 2007, MNRAS, 377, 41
Davé R., Oppenheimer B. D., Sivanandam S., 2008, MNRAS, 391, 110
De Lucia G., Blaizot J., 2007, MNRAS, 375, 2
Eisenhardt P. R. M. et al., 2008, ApJ, 684, 905
Eke V. R., Navarro J. F., Frenk C. S., 1998, ApJ, 503, 569
Ettori S., Dolag K., Borgani S., Murante G., 2006, MNRAS, 365, 1021
Ettori S., Morandi A., Tozzi P., Balestra I., Borgani S., Rosati P., Lovisari L., Terenziani F., 2009, A&A, 501, 61
Evrard A. E., Henry J. P., 1991, ApJ, 383, 95
Fabjan D., Borgani S., Tornatore L., Saro A., Murante G., Dolag K., 2010, MNRAS, 401, 1670
Feldmeier J. J., Mihos J. C., Morrison H. L., Rodney S. A., Harding P., 2002, ApJ, 575, 779
Feldmeier J. J., Mihos J. C., Morrison H. L., Harding P., Kaib N., Dubinski J., 2004, ApJ, 609, 617
Giodini S. et al., 2009, ApJ, 703, 982 (GPF09)
Gonzalez A. H., Zabludoff A. I., Zaritsky D., Dalcanton J. J., 2000, ApJ, 536, 561
Gonzalez A. H., Zabludoff A. I., Zaritsky D., 2005, ApJ, 618, 195
Gonzalez A. H., Zaritsky D., Zabludoff A. I., 2007, ApJ, 666, 147 (GZZ07)
Horner D. J., Perlman E. S., Ebeling H., Jones L. R., Scharf C. A., Wegner G., Malkan M., Maughan B., 2008, ApJS, 176, 374
Kaiser N., 1991, ApJ, 383, 104
Kay S. T., da Silva A. C., Aghanim N., Blanchard A., Liddle A. R., Puget J.-L., Sadat R., Thomas P. A., 2007a, MNRAS, 377, 317
Kay S. T., da Silva A. C., Aghanim N., Blanchard A., Liddle A. R., Puget J.-L., Sadat R., Thomas P. A., 2007b, MNRAS, 377, 317
Kitzbichler M. G., White S. D. M., 2008, MNRAS, 391, 1489
Komatsu E. et al., 2010, preprint (arXiv e-prints: 1001.4538)
Kravtsov A. V., Nagai D., Vikhlinin A. A., 2005, ApJ, 625, 588
Krick J. E., Bernstein R. A., Pimbblet K. A., 2006, ApJ, 131, 168
Laganá T. F., Lima Neto G. B., Andrade Santos F., Cypriano E. S., 2008, A&A, 485, 633 (LLA08)
LaRoque S. J., Bonamente M., Carlstrom J. E., Joy M. K., Nagai D., Reese E. D., Dawson K. S., 2006, ApJ, 652, 917
McCarthy I. G. et al., 2009, MNRAS, 406, 822
Mantz A., Allen S. W., Ebeling H., Rapetti D., Drlica-Wagner A., 2009a, MNRAS, 406, 1773
Mantz A., Allen S. W., Rapetti D., Ebeling H., 2009b, MNRAS, 406, 1759
Maughan B. J., Jones C., Forman W., Van Speybroeck L., 2008, ApJS, 174, 117
Mazzotta P., Rasia E., Moscardini L., Tormen G., 2004, MNRAS, 354, 10
Meneghetti M., Rasia E., Merten J., Bellagamba F., Ettori S., Mazzotta P., Dolag K., 2009, A&A, 514, A93
Mo H. J., Yang X., van den Bosch F. C., Katz N., 2005, MNRAS, 363, 1155
Muanwong O., Thomas P. A., Kay S. T., Pearce F. R., 2002, MNRAS, 336, 527
Muanwong O., Kay S. T., Thomas P. A., 2006, ApJ, 649, 640
Nagai D., Kravtsov A. V., Vikhlinin A., 2007, ApJ, 668, 1
Navarro J. F., Frenk C. S., White S. D. M., 1995, MNRAS, 275, 720
Navarro J. F., Frenk C. S., White S. D. M., 1997, ApJ, 490, 493
Pearce F. R., Thomas P. A., Couchman H. M. P., 1994, MNRAS, 268, 953
Piffaretti R., Valdarnini R., 2008, A&A, 491, 71
Ponman T. J., Sanderson A. J. R., Finoguenov A., 2003, MNRAS, 343, 331
Pratt G. W., Arnaud M., Pointecouteau E., 2006, A&A, 446, 429
Pratt G. W. et al., 2010, A&A, 511, A85
Puchwein E., Springel V., Sijacki D., Dolag K., 2010, preprint (arXiv e-prints: 1001.3018)
Rasia E. et al., 2006, MNRAS, 369, 2013
Sadat R. et al., 2005, A&A, 437, 31
Sanderson A. J. R., Ponman T. J., Finoguenov A., Lloyd-Davies E. J., Markevitch M., 2003, MNRAS, 340, 989
Short C. J., Thomas P. A., 2009, ApJ, 704, 915
Short C. J., Thomas P. A., Young O. E., Pearce F. R., Jenkins A., Muanwong O., 2010, MNRAS, 408, 2213
Spergel D. N. et al., 2003, ApJS., 148, 175
Springel V. et al., 2005, Nat., 435, 629
Stanek R., Rasia E., Evrard A. E., Pearce F., Gazzola L., 2010, ApJ, 715, 1508
Sun M., Voit G. M., Donahue M., Jones C., Forman W., Vikhlinin A., 2009, ApJ, 693, 1142
Sutherland R. S., Dopita M. A., 1993, ApJS, 88, 253
Tornatore L., Borgani S., Springel V., Matteucci F., Menci N., Murante G., 2003, MNRAS, 342, 1025
Tozzi P., Rosati P., Ettori S., Borgani S., Mainieri V., Norman C., 2003, ApJ, 593, 705

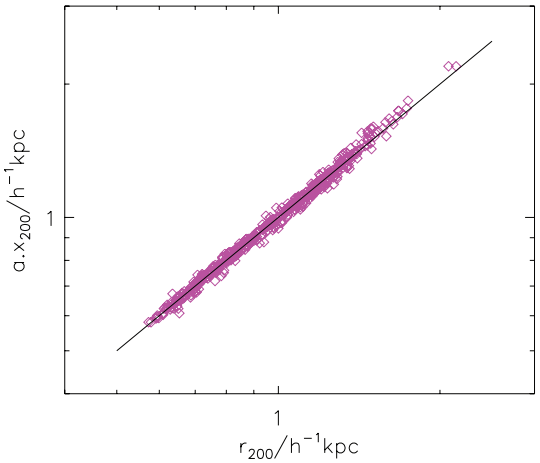

Figure A1. The abscissa shows the actual value of r_{200} for each of the clusters, whilst the ordinate shows the value predicted from M_{2500} and M_{500} assuming an NFW profile.

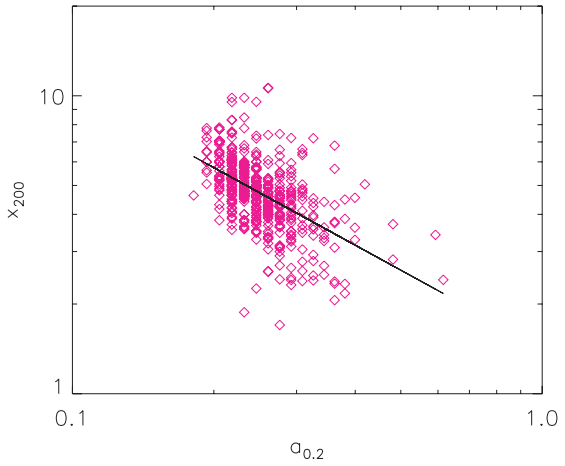

Figure A2. Cluster concentration versus the expansion factor at the time that the clusters have accumulated one-fifth of their final mass. The solid line shows the best-fitting power-law correlation.

Vikhlinin A., Kravtsov A., Forman W., Jones C., Markevitch M., Murray S. S., Van Speybroeck L., 2006, ApJ, 640, 691
Voit G. M., Kay S. T., Bryan G. L., 2005, MNRAS, 364, 909
Weiner B. J. et al., 2009, ApJ, 692, 187
Zibetti S., White S. D. M., Schneider D. P., Brinkmann J., 2005, MNRAS, 358, 949

APPENDIX A

The central concentration of clusters can be determined by measuring the mass at two different overdensities, for example M_{2500} and M_{500}. Together, these uniquely determine the parameters of the NFW profile (Navarro, Frenk & White 1997) without any need to fit the profile as a function of radius.[2] To test the effectiveness of this procedure, we show in Fig. A1 the value of r_{200} predicted by the NFW fit (i.e. the NFW scale radius, a, times the concentration, x_{200}) versus the actual value. As can be seen, the two agree very well, confirming that the clusters are well fit by the NFW profile out to this radius.

Cluster concentrations are often thought to have a dependence upon cluster mass, with more massive clusters having lower concentrations. That is indeed the case, but we find a much stronger correlation with cluster formation time, as illustrated in Fig. A2. Here the formation time is taken to be the value of the expansion factor when the total mass of all the subhaloes that will go on to make up the cluster equal one-fifth of the final cluster mass, but other definitions give similar correlations. We plot expansion factor rather than age as this gives a more linear correlation. The results are shown here for the GO simulation; those for the PC and FO runs are very slightly different because of the contribution of the baryons to the total mass.

On removing the best-fitting correlation (shown as a solid line in the figure), the residual concentration shows no dependence on mass. The correlation with mass is thus a secondary one that follows because low-mass clusters tend to form at lower expansion factors than more massive ones.

[2] We provide IDL routines to do this at http://astronomy.susx.ac.uk/~petert/nfw.pro.

This paper has been typeset from a TEX/LATEX file prepared by the author.